



Tuning the catalytic performance of Ni-catalysed dry reforming of methane and carbon deposition via Ni-CeO_{2-x} interaction

Maoshuai Li^{a,b,*}, André C. van Veen^{b,*}

^a College of Materials Science & Engineering, Shenzhen University, Shenzhen 518060, China

^b School of Engineering, The University of Warwick, Coventry CV4 7AL, United Kingdom

ARTICLE INFO

Keywords:

Methane dry reforming
Ni/CeO₂
Metal-oxide interaction
Decoration
Carbon deposition

ABSTRACT

The role of tuning metal-support interaction in determining the catalytic activity and carbon formation in dry reforming of methane to syngas was examined over CeO₂ supported Ni nanoparticles. The catalysts pre- and post- reaction were subjected to characterisation in terms of N₂ physisorption, TPR, XRD, TEM, XPS and TGA-DTG. Reduction of Ni/CeO₂ in H₂ in the temperature range (773–973 K) generated a strong bonding between Ni and CeO₂ that inhibited Ni particle sintering (8.7–9.4 nm). High-temperature (≥ 873 K) reduction induced decoration/encapsulation of Ni nanoparticles by a thin layer of reduced ceria support with partial coverage of Ni surface. The decoration/encapsulation effect strongly influences the catalytic properties of Ni, which enables to tune the catalytic activity of Ni/CeO₂ and carbon deposition in dry reforming of methane.

1. Introduction

In supported metal catalysis, strong support (generally oxides) and metal interaction (SMSI) including electron transfer, support decoration of metal nanoparticles and cluster stabilisation can often determine catalytic reactivity and/or selectivity [1,2]. Ceria is a typical case of oxide support that is facile to generate interaction with the supported metal (e.g., Pd, Ru and Rh) phase following thermal activation in H₂ [3]. A number of studies have reported metal-ceria interaction serves to increase rates or control product selectivity for reactions involving redox steps (e.g., CO oxidation over Pt/CeO₂ [4], water gas shift over Pt/CeO₂ [5], Au/CeO₂ [6]) and CO₂ hydrogenation over Cu/CeO₂ [7].

Dry reforming of methane to syngas, an intermediate for synthesis of methanol and Fischer-Tropsch products, is a promising route for conversion of methane to value-added chemicals/fuels and reduction of greenhouse gas (e.g., CO₂ and CH₄) emission. This reaction has been experimentally and theoretically studied over noble (Pt [8], Ru [9], Rh [10–12] and Pd [13]), non-noble metal (Ni [14–17] and Co [18]) and bimetallic (NiCo [19], FeNi [20], PdNi [21] and NiPt [22]) catalysts. Inexpensive Ni-based catalysts exhibited comparable activity to noble metals due to the outstanding capacity for activation/dissociation of the C–H bond of methane [23]. There is a consensus that methane activation is the rate-determining step in the dry reforming of methane [24]. Metal-support interaction is critical in determining adsorption/dissociation of methane. A search through literature found that Liu et al. [25] studying dry reforming of methane over Ni-CeO₂ (111)

surfaces using in situ XPS and DFT calculation, demonstrated strong metal-support interaction can activate Ni for methane dissociation at 300 K. Higher catalytic stability of Ni/CeO₂ in dry reforming of methane (1023 K) relative to steam reforming was linked to strong metal-support interaction on the basis of in situ XAS and XANES analysis [26]. The degree of metal-support interaction can modify the characteristics of the supported metal phase and reactant adsorption. SMSI can alter the metal electronic properties via charge transfer between metal and support, stabilise small metal clusters in support surface vacancies and induce support decoration of metal surface via migration of support oxide to the metal particles [1,2]. Moreover, solid solutions can be generated via dissolution of metal in support oxide lattice. It is known that SMSI-induced decoration/encapsulation of metal nanoparticles contributes to suppression of H₂ and CO chemisorption over reducible oxides (e.g., TiO₂, CeO₂ and CeTbO_x) supported noble metals (e.g., Ru, Rh and Pt) [27–30]. In the reported studies up to date the influence of Ni-CeO₂ interaction on the morphology of Ni particles and activation of CH₄ and CO₂ in dry reforming have not been studied to any significant extent. In this study, we examine the impact of SMSI-induced decoration/encapsulation of Ni particles on the catalytic response in dry reforming of methane over CeO₂ supported Ni. Carbon deposition was studied as one critical consideration for the decoration/encapsulation effect on the catalyst stability.

* Corresponding authors at: School of Engineering, The University of Warwick, Coventry CV4 7AL, United Kingdom.

E-mail addresses: maoshuailli@szu.edu.cn (M. Li), Andre.vanVeen@warwick.ac.uk (A.C. van Veen).

<https://doi.org/10.1016/j.apcatb.2018.06.032>

Received 17 April 2018; Received in revised form 4 June 2018; Accepted 11 June 2018

Available online 20 June 2018

0926-3373/© 2018 Elsevier B.V. All rights reserved.

2. Experimental

2.1. Materials and catalyst preparation

Commercial CeO₂ (Sigma-Aldrich) was used as received. (5% w/w) Ni on CeO₂ was prepared by wet-impregnation. CeO₂ (5 g) was added to aqueous solution of Ni(NO₃)₂ (Alfa Aesar, 98%, 9×10^{-2} M, 50 cm³) and stirred (500 rpm) at room temperature overnight. The solid was obtained by evaporation and dried in air at 393 K overnight. The resultant sample was sieved (ATM fine test sieves) to mean particle diameter = 75 μm, activated at 773–973 K in H₂ (10 cm³ min⁻¹) for 1 h, cooled to ambient temperature and passivated in 1% v/v O₂/N₂ for 1 h for *ex situ* characterisation (including N₂ physisorption, XRD and HRTEM).

2.2. Catalyst characterisation

Nitrogen physisorption was performed on the Micromeritics ASAP 2020 system. Specific surface area (SSA) and pore volume were calculated using the standard BET method and BJH desorption, respectively. Prior to analysis, samples were vacuumed and outgassed at 573 K for 1 h. Temperature programmed reduction (TPR) was conducted in a quartz tube cell. The sample (Ni precursor on CeO₂) was heated in 84 cm³ min⁻¹ 5% v/v H₂/Ar at 10 K min⁻¹ to 1073 K. Hydrogen consumption was monitored by a thermal conductivity detector (TCD). X-ray diffractograms (XRD) were recorded on a Bruker D5000 X-ray diffractometer using Cu Kα radiation. Samples were scanned at 0.01° step⁻¹ over the range 20° ≤ 2θ ≤ 80° at ambient temperature and the diffractograms identified against the JCPDS-ICDD reference standards. Metal particle morphology (size and shape) was examined by high resolution transmission electron microscopy (HRTEM, JEOL 2100 LaB6), employing Gatan Digital Micrograph for data acquisition/manipulation. Samples for analysis were prepared by dispersion in ethanol and deposited on a holey carbon/Cu grid. Mean Ni size (*d*) was obtained from a count of at least 200 particles. XPS measurement of the reduced sample was performed on a Kratos Axis Ultra DLD spectrometer using a monochromated Al Kα X-ray source. The Ni 2p_{3/2} and Ce 3d spectra were collected. Characteristic Ni 2p_{3/2} binding energy (BE) for metallic Ni is 852.5 eV and 856.3 eV; for NiO is 853.7 eV, 855.4 eV and 861.0 eV [31]. The BE scale was calibrated by adventitious carbon (BE = 285.0 eV). The data were analysed in CasaXPS, using Shirley backgrounds, mixed Gaussian-Lorentzian (Voigt) line shapes and asymmetry parameters where appropriate. The fixed positions of the components were similar to those reported elsewhere [31]. The peak asymmetry was defined in the form of LA (α, β, *m*), where α and β refer to the spread of the tail on each side of the Lorentzian component; *m* is the width of the Gaussian for convolution of the Lorentzian line. The surface element composition was calculated from the peak area. Thermogravimetric-derivative thermogravimetric analysis (TGA-DTG) of the spent Ni/CeO₂ catalysts for evaluation of carbon deposition was carried out on a thermal analyser (NETZSCH STA449). The samples (ca. 10–20 mg) were heated in 50 cm³ min⁻¹ air to 973 K (at 10 K min⁻¹).

2.3. Catalyst testing

Dry reforming of methane was carried out at atmospheric pressure after *in situ* activation in a continuous flow fixed bed tubular reactor (10 mm i.d.). Reactions were conducted under operating conditions that ensured negligible mass/heat transport limitations. Isothermal conditions (± 1 K) were ensured by diluting the catalyst bed with ground glass (75 μm); the ground glass was mixed thoroughly with catalyst before loading into the reactor. Reaction temperature was continuously monitored by a thermocouple inserted in the catalyst bed. A co-current flow of CO₂ (BOC, 99.99%), CH₄ (BOC, 99.99%), N₂ (BOC, 99.99%) and Ar (BOC, 99.99%) was introduced to reactor by Brooks

mass flow controller (SLA5800 series) at gas hourly space velocity (GHSV) = 4.8×10^4 h⁻¹. 10–40% (vol.%) CH₄ was diluted in N₂ and Ar. Inlet CH₄ to CO₂ feeding rate was fixed at 1:1. 0.03 g catalyst was used in the reforming reaction. The molar Ni to inlet CH₄ feeding rate *n*/F_{CH₄} was 4.8×10^{-3} h. The reactor effluent was analysed using online gas chromatography (Shimadzu 2014) equipped with a 0.5 cm³ sampling loop, thermal conductive detector (TCD) and flame ionization detector (FID), employing serial Haysep Q (3.0 m × 2.1 mm i.d.) and Molecular Sieve 5 A packed columns (2.0 m × 2.1 mm i.d.). Data acquisition and manipulation were performed using GCsolution Lite (Version 2.4) chromatography data system. Reactant *i* (*i* = CH₄ or CO₂) fractional conversion (*X_i*) is calculated by

$$X_i = \frac{F_{[reactant]i,in} - F_{[reactant]i,out}}{F_{[reactant]i,in}} \quad (1)$$

Reactant (*i*) consumption rate (*R_i*, h⁻¹) was obtained from:

$$R_i = \frac{F_{[reactant]i,in} \times X_{i,s}}{n} \quad (2)$$

where subscripts “in” and “out” refer to inlet and outlet gas streams; “*n*” refers to mole number of Ni; “*X_{i,s}*” refers to steady-state conversion. The inlet fractional concentration was defined by the molar flow rate of reactant to the total flow rate. In blank tests, passage of CH₄ and CO₂ through the empty reactor or over support alone did not result in any detectable conversion. Repeated reactions delivered data reproducibility and carbon balance within 7%.

3. Results and discussion

3.1. Catalyst characterisation

Ni/CeO₂ post-reduction at 773 K exhibited a SSA (11 m² g⁻¹, Table 1), close to that (9 m² g⁻¹) reported in the literature [32]. Reduction at higher temperature (773 → 973 K) resulted in a loss of SSA and pore volume (Table 1), which can be linked to grain sintering and agglomeration [33]. TPR profiles of CeO₂ support and Ni precursor on CeO₂ are presented in Fig. 1. Thermal treatment of ceria (I) generated two broad peaks at 742 K and 1148 K that can be linked to surface (720–790 K) and bulk (> 1059 K) reduction [34,35]. TPR analysis of Ni precursor on CeO₂ (II) generated multiple signals. The sharp TPR peaks with associated temperature maxima (*T_{max}*) of 582 K and 587 K can be attributed to the decomposition of nickel precursor to NiO. Moraes et al. [36] studying the reducibility behaviour of Ni/CeO₂, ascribed a TPR peak (*T_{max}* = 588 K) to the decomposition of nickel nitrate. A subsequent reduction of NiO to metallic Ni was responsible for the higher *T_{max}* peak (616 K) recorded in this study. Mahammadunnisa [37] and Moraes [36] have attributed reduction peaks with *T_{max}* in the temperature range of 588–653 K to reduction of NiO in the TPR analysis of 5–10% Ni/CeO₂ (w/w). Hydrogen consumption signals at *T_{max}* = 706 K and at the extended isothermal hold (1073 K) can be linked to surface and bulk reduction of ceria, where addition of Ni to CeO₂ lowered the requisite temperature. Structure analysis by XRD generated diffraction patterns are shown in Fig. 2. Diffraction signals at 2θ = 44.5° can be attributed to Ni (111). The peak intensity increased with increasing reduction temperature. In addition to Ni signals, diffraction peaks at 2θ = 28.6°, 33.2°, 47.6°, 56.4°, 59.2°, 69.6°, 76.8° and 79.2° can be

Table 1
Effect of reduction temperature on SSA and pore volume of Ni/CeO₂ pre- and post-reaction.

Sample		773 K	873 K	973 K
Pre-reaction	SSA (m ² g ⁻¹)	11	8	8
	Pore volume (cm ³ g ⁻¹)	0.032	0.024	0.024
Post-reaction	SSA (m ² g ⁻¹)	21	10	8
	Pore volume (cm ³ g ⁻¹)	0.036	0.021	0.025

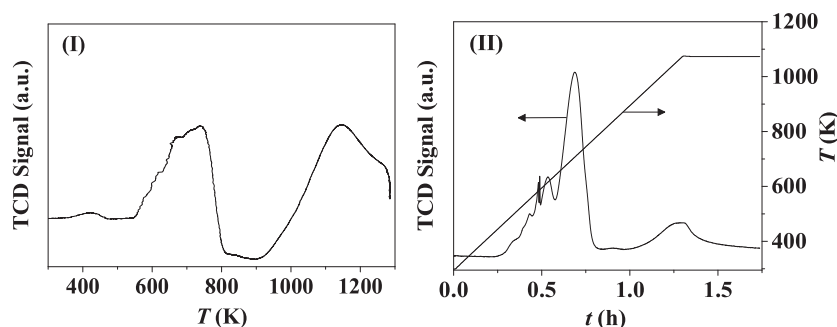


Fig. 1. Temperature programmed reduction (TPR) profiles for (I) CeO₂ and (II) Ni/CeO₂.

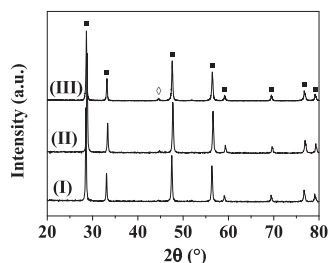


Fig. 2. XRD patterns for Ni/CeO₂ reduced at (I) 773 K, (II) 873 K and (III) 973 K (○: Ni; ■: CeO₂).

attributed to face-centred cubic CeO₂. There was no detectable phase due to Ce₂O₃.

The morphology of Ni nanoparticles of the activated Ni/CeO₂ catalysts was characterised by TEM. HRTEM image of Ni/CeO₂ activated at 773 K (Fig. 3(AI)) showed a number of Ni nanocrystallites with exposed (111) facet were distributed on the surface of CeO₂. A clear interface boundary was observed between Ni and CeO₂ (dotted frame), suggesting strong metal-support interaction. The Ni particles were in nanoscale (3–22 nm) with a mean size of 8.7 nm (AII). Reduction of Ni/CeO₂ at higher temperature (873 K) resulted in decoration/encapsulation of Ni nanoparticles by a thin layer of ceria with a decreased exposure of Ni (111) surface (BI). A reduction of metal oxide support can cause a rupture of the oxide lattice with substoichiometric oxygen concentration that can induce migration of the reduced oxide to the top of metal surface via grain boundaries between metal and support [1,2]. It has been reported that thermal (≥ 573 K) treatment of (e.g., TiO₂ and CeO₂) supported noble metals (e.g., Rh, Ru, Au and Pt) in H₂ can induce migration of metal oxides from reduced support to the supported metal phase, generating decoration/encapsulation effect on the supported metal nanoparticles [29,30,38]. Our results present this effect also applies to reducible oxide supported non-noble metal (e.g., Ni/CeO₂), where higher thermal treatment temperature (≥ 873 K) was required. Larger Ni sizes (3–22 nm, mean = 9.2 nm) were observed over Ni/CeO₂ (BII) due to slight sintering/agglomeration of Ni nanoparticles after reduction at 873 K. The Ni/CeO₂ catalyst activated at 973 K (CI) suffered severe decoration/encapsulation of Ni nanoparticles leading to a higher coverage of Ni surface by ceria. This suggests higher reduction temperature further promoted migration of ceria to Ni surface. It should be noted that Ni particle sizes (3–21 nm, mean = 9.4 nm, (CII)) were similar to that recorded over the catalyst reduced at 873 K. This can be attributed to stronger interaction between metal and support stabilised Ni nanoparticles and inhibited sintering [39].

Ni/CeO₂ post-reduction at 773 K and 973 K as representatives was subjected to XPS analysis. Spectra over Ni 2p_{3/2} (A) and Ce 3d (B) BE regions are shown in Fig. 4. Ni 2p_{3/2} spectrum for both samples exhibited common signals at 852.5 eV, consistent with the reference metallic Ni (852.4–852.6 eV) [40]. Multi-split peaks at 853.7 eV, 855.8 eV and 861.1 eV match the characteristic Ni 2p_{3/2} BE of NiO (core level:

853.7 eV, 855.7 eV; satellite: 861.0 eV) [31,41]. The formation of NiO resulted from oxidation of metallic Ni when exposed to air [40]. An additional core level peak at 856.9 eV with a satellite peak at 861.7 eV, which was a contribution of Ni²⁺ species that was bonded with ceria (Ni–O–Ce) at the interface. The spectrum of Ce 3d (B) showed up to ten signal components due to various final state electron configurations [42]. The peaks (denoted ν , ν_0 , ν' , ν'' and ν''') are linked to Ce 3d_{5/2}; while the signals (μ , μ_0 , μ' , μ'' and μ''') correspond to Ce 3d_{3/2}. Ce⁴⁺ species generates peaks μ''' and ν''' , μ'' and ν'' , μ and ν due to Ce3d⁹4f⁰O2p⁶, Ce3d⁹4f¹O2p⁵ and Ce3d⁹4f²O2p⁴ final state, respectively [43]. Ce³⁺ component was associated with the signals μ' and ν' corresponding to Ce3d⁹4f¹O2p⁶ state, μ_0 and ν_0 resulting from Ce3d⁹4f²O2p⁵ state [43]. Surface element composition analysis (Table 2) revealed higher reduction temperature resulted in a lower content of nickel species (Ni⁰ and Ni²⁺), a higher concentration of Ce components (Ce³⁺ and Ce⁴⁺) and of oxygen, and a lower ratio of Ni/Ce. This can be attributed to decoration/encapsulation of Ni nanoparticles by ceria layer leading to lower Ni surface exposure. In addition, larger fractions of Ce³⁺ (18.8% → 22.2%) and metallic Ni⁰ (16.3% → 26.4%) were observed at higher reduction temperature.

3.2. Catalytic response

Representative time on-stream conversions of CH₄ and CO₂, and H₂/CO ratio in dry reforming of methane (773 K) over Ni/CeO₂ (using reduction temperature (T_{reduce}) = 773 K) is presented in Fig. 5. The catalyst exhibited stable conversion (ca. 0.30) for CH₄; while a temporal loss in CO₂ conversion was observed with steady state (ca. 0.42) attained after 5 h on-stream. Our conversions are higher than that X_{CH₄} = 0.22–0.31, X_{CO₂} = 0.20–0.30 reported for reaction over Ni/CeO₂ at higher temperature (823 K) and lower GHSV (3.6 × 10⁴ h^{−1}) [44]. CH₄ and CO₂ were converted to syngas with no detectable by-products (e.g., alkane and/or alkene). H₂/CO ratio was in the range of 0.70–0.76 with a value of 0.70 at the steady state.

To explore how Ni–CeO₂ interaction impacts on the adsorption/activation of CH₄ and CO₂, Ni/CeO₂ was reduced at different temperatures (773–973 K) and examined in dry reforming of methane (773 K). Reaction over Ni/CeO₂ (reduced at 773 K) delivered a consumption rate for CH₄ (64 h^{−1}), lower than that of CO₂ (89 h^{−1}). An increase in reduction temperature (773 → 973 K) resulted in lower conversion rates for both CH₄ and CO₂ (Fig. 6), suggesting decoration/encapsulation of Ni nanoparticles did not facilitate conversion of CH₄ and CO₂. The influence of decoration/encapsulation of Ni particles on the catalytic activity of Ni/CeO₂ in dry reforming of methane has not been studied well in the literature. But we can note Lustemberg et al. [45] investigating the effect of Ni coverage on the catalytic activity of Ni–CeO₂ (111) surfaces for CH₄ activation (300 K) observed a dramatic drop in CH₄ dissociation at coverage > 0.2 ML. Wang et al. [46] demonstrated embedding of Ir species into Ce_{0.9}Pr_{0.1}O₂ support did not favour activation of CH₄ and CO₂ in dry reforming of methane over Ir/Ce_{0.9}Pr_{0.1}O₂. It has been reported that CH₄ is activated/dissociated on

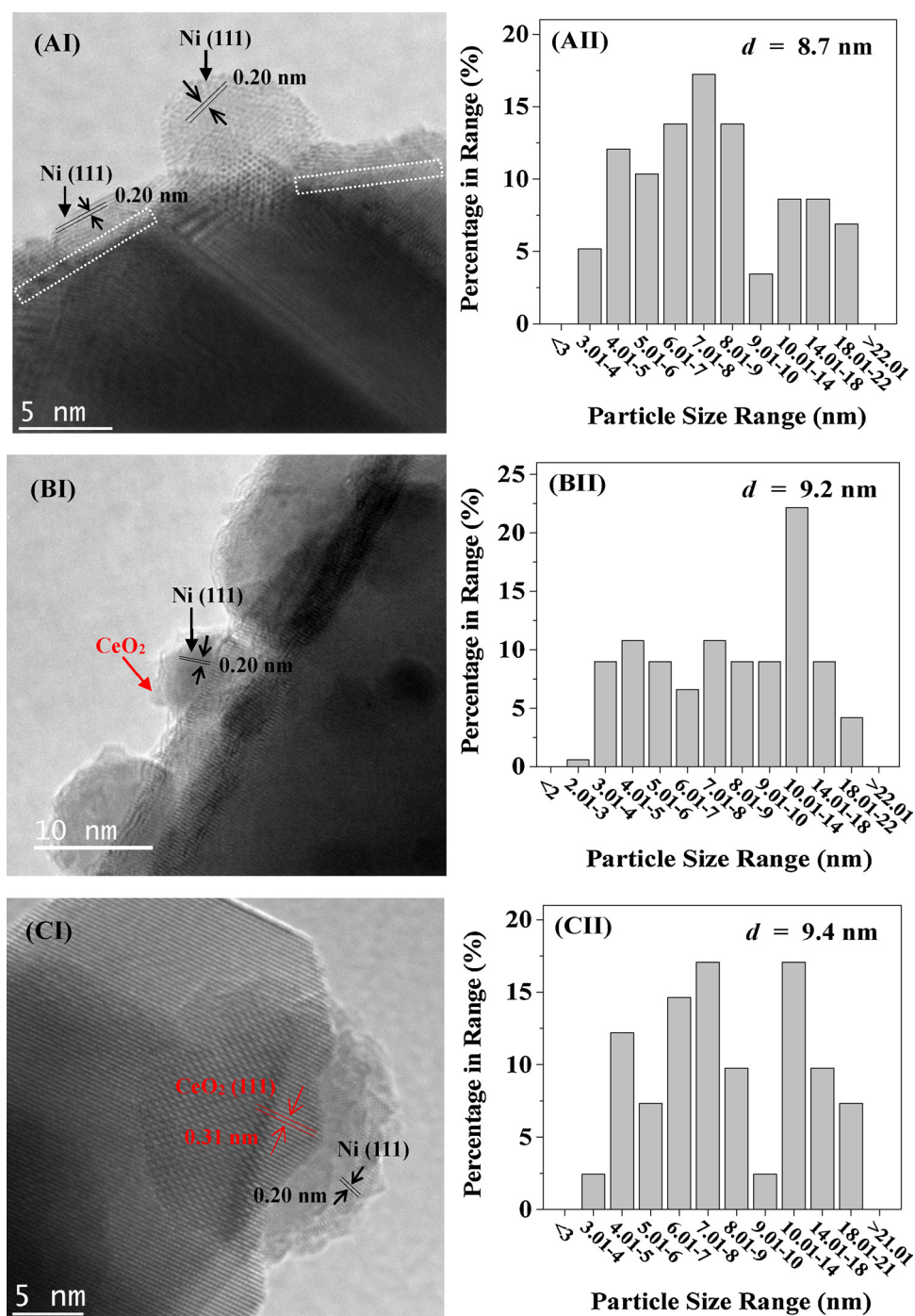


Fig. 3. (I) Representative HRTEM images for Ni/CeO₂ reduced at (A) 773 K, (B) 873 K and (C) 973 K with (II) associated Ni particle size distribution histograms.

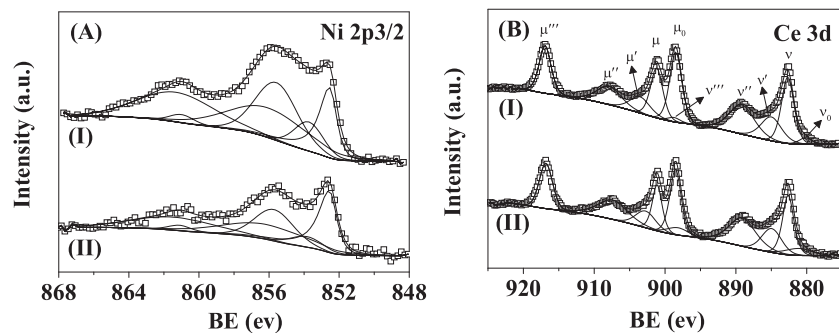
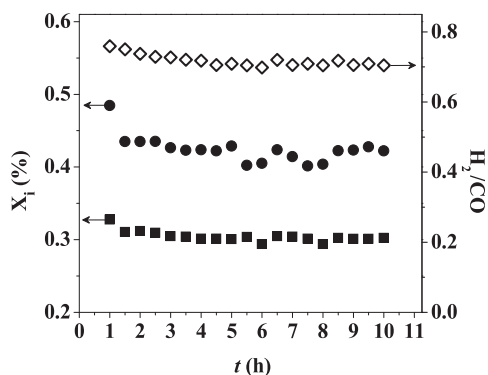
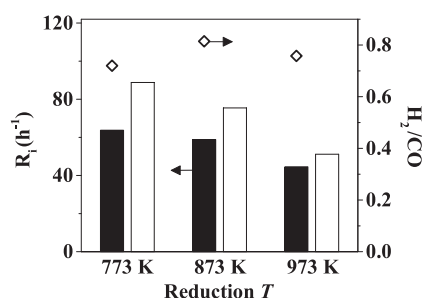
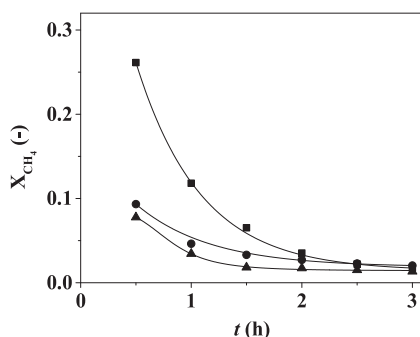


Fig. 4. XPS profile of (A) Ni 2p_{3/2} and (B) Ce 3d for Ni/CeO₂ reduced at (I) 773 K and (II) 973 K.

Table 2Surface element composition, Ni/Ce ratio and content of Ce^{3+} , Ce^{4+} , Ni^0 and Ni^{2+} determined from XPS analysis for activated Ni/CeO₂.

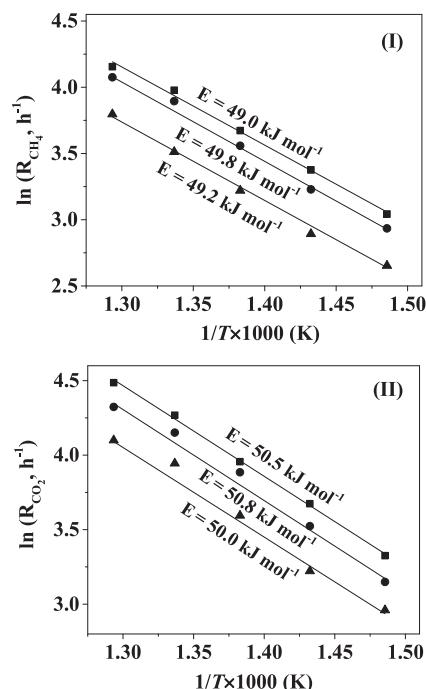
Sample	Ce (%)	Ni (%)	O (%)	Ni/Ce	Ce^{3+} (%)	Ce^{4+} (%)	Ni^0 (%)	Ni^{2+} (%)
Ni/CeO ₂ -773 K	20.0	15.5	64.5	0.78	18.8	81.2	16.3	83.7
Ni/CeO ₂ -973 K	25.0	7.1	67.9	0.28	22.2	77.8	26.4	73.6

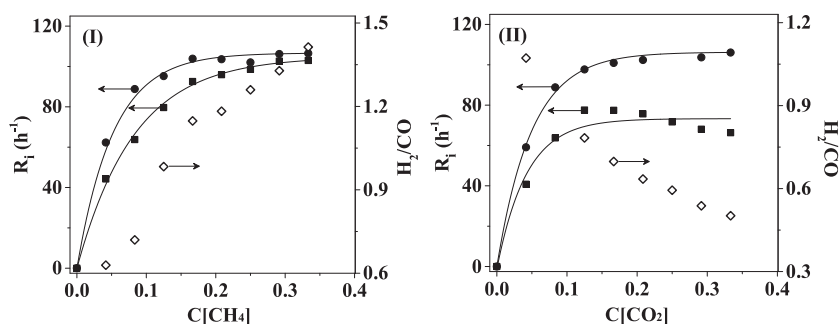
**Fig. 5.** Time on-stream conversion of CH₄ (■) and CO₂ (●) and H₂/CO (◇) in dry reforming of methane over Ni/CeO₂. Reaction condition: $T_{\text{react}} = 773$ K, $T_{\text{reduce}} = 773$ K, $P = 1$ atm, $\text{GHSV} = 4.8 \times 10^4 \text{ h}^{-1}$, $n/\text{F}_{\text{CH}_4} = 4.8 \times 10^{-3} \text{ h}$.**Fig. 6.** Effect of reduction temperature (773–973 K) on the reactant consumption rate (R_i ; solid: CH₄, open: CO₂) and H₂/CO (◇) in dry reforming of methane over Ni/CeO₂. Reaction condition: $T_{\text{react}} = 773$ K, $P = 1$ atm, $\text{GHSV} = 4.8 \times 10^4 \text{ h}^{-1}$, $n/\text{F}_{\text{CH}_4} = 4.8 \times 10^{-3} \text{ h}$.**Fig. 7.** Variation of time on-stream conversion with reduction temperature (■: 773 K, ●: 873 K, ▲: 973 K) in the methane decomposition over Ni/CeO₂. Reaction condition: $T_{\text{react}} = 773$ K, $P = 1$ atm, $\text{GHSV} = 4.8 \times 10^4 \text{ h}^{-1}$, $n/\text{F}_{\text{CH}_4} = 4.8 \times 10^{-3} \text{ h}$.

active metal surface; while CO₂ binds on support and metal-support interface in dry reforming of methane over reducible oxide supported metal catalysts [24,46,47]. Higher coverage of Ni particles by ceria layer due to encapsulation effect must decrease Ni surface exposure and metal-oxide boundary perimeter for adsorption/activation of CH₄ and CO₂. Moreover, a lower content of surface Ni species (Table 2) can contribute to the decreased activity observed at higher reduction

temperature. Regarding H₂/CO, the reaction using reduction temperature = 873 K delivered higher H₂/CO ratio (0.81) than that (0.72–0.76) at 773 K and 973 K. The methane decomposition (773 K) was examined over Ni/CeO₂ to further probe the effect of decoration/encapsulation of Ni nanoparticles on CH₄ activation. The variation of time on-stream conversion of CH₄ with reduction temperature is presented in Fig. 7. Regardless of reduction temperature, a rapid loss of CH₄ conversion was observed within 3 h on-stream. An increase in reduction temperature resulted in lower conversions for CH₄, in agreement with that observed in dry reforming of methane (Fig. 6). This further confirmed high coverage of Ni surface by support resulting from encapsulation of Ni particles decreases the catalytic capacity of Ni/CeO₂ for CH₄ activation/dissociation.

Arrhenius plots using conversion rates of CH₄ and CO₂ for dry reforming of methane over Ni/CeO₂ (reduced at 773 K, 873 K and 973 K, respectively) are presented in Fig. 8. An increase in reaction temperature from 673 K to 773 K resulted in higher conversion rates for CH₄ and CO₂, consistent with the nature of endothermic reaction. Reactions using higher reduction temperature delivered lower conversion rates at each reaction temperature, in agreement with that observed in Fig. 6. This again confirmed decoration/encapsulation of Ni nanoparticles over Ni/CeO₂ does not favour adsorption/activation of CH₄ and CO₂. Apparent activation energies for CH₄ extracted from the Arrhenius plots (Fig. 8(I)) were close to each other (49.0–49.8 kJ mol⁻¹). The values fall in the range (41.8–62.7 kJ mol⁻¹) reported for the reaction over (Al₂O₃, Al₂O₃-CeO₂, La₂O₃, SiO₂ and ZrO₂) supported Ni catalysts [48]. Apparent activation energies for CO₂ (50.0–50.8 kJ mol⁻¹) were higher than that of CH₄ (Fig. 8(II)). The values are in agreement with that

**Fig. 8.** Arrhenius plots in terms of CH₄ (I) and CO₂ (II) conversion rate in dry reforming of methane over Ni/CeO₂ reduced at different temperatures (■: 773 K, ●: 873 K, ▲: 973 K). Reaction condition: $P = 1$ atm, $\text{GHSV} = 4.8 \times 10^4 \text{ h}^{-1}$, $n/\text{F}_{\text{CH}_4} = 4.8 \times 10^{-3} \text{ h}$.



reported for reaction over Ni/Al₂O₃ (56.1 kJ mol⁻¹) [49] and Ni/Al₂O₃-CeO₂ (46.2 kJ mol⁻¹) [50].

The effect of inlet fractional concentration of CH₄ (C [CH₄]) and CO₂ (C [CO₂]) on the conversion rate and H₂/CO ratio in dry reforming of methane was examined over Ni/CeO₂. The conversion rate for CH₄ and CO₂ increased dramatically with increasing the fractional concentration up to 0.125 and followed by a slow increase at higher concentration (Fig. 9), in agreement with that reported for reaction over Ni-La₂O₃@SiO₂ [51]. H₂/CO increased (0.62 → 1.42) with an increase in CH₄ concentration, suggesting greater H₂ generated at higher CH₄ feeding; while an increase in CO₂ concentration resulted in a decrease in H₂/CO (1.07 → 0.50). Reaction order for CH₄ and CO₂ was estimated from the variation in conversion rates (R_i) with inlet reactant concentration. The reactant (CH₄ and CO₂) conversion rates are expressed by the semi-empirical equations (Eqs. (3) and (4)) as described elsewhere [52].

$$R_{\text{CH}_4} = k_1 [\text{CH}_4]^{\alpha_1} [\text{CO}_2]^{\beta_1} \quad (3)$$

$$R_{\text{CO}_2} = k_2 [\text{CH}_4]^{\alpha_2} [\text{CO}_2]^{\beta_2} \quad (4)$$

A calculation treatment of Eq. (3) using natural logarithm found the reaction orders for CH₄ (α₁) and CO₂ (β₁) are 0.534 and 0.373, respectively. The reaction orders in Eq. (4) for CH₄ (α₂) and CO₂ (β₂) are 0.592 and 0.471, respectively. The values are close to that reported in the existing study [51].

3.3. Catalyst characterisation post-reaction

Carbon deposition and Ni sintering often result in catalyst deactivation in the methane reforming reaction. To study the encapsulation effect of Ni particles on catalyst deactivation, Ni/CeO₂ catalysts post-reaction (773 K) were subjected to characterisation in terms of N₂ physisorption, XRD, TEM and TGA-DTG analysis. Ni/CeO₂ pre-reduced at 773 K and 873 K exhibited an increase in SSA and a decrease in pore volume post-reaction (Table 1), which can be attributed to carbon accumulation. The spent Ni/CeO₂ (reduced at 973 K) showed a SSA and pore volume that were close to the values recorded for the fresh catalyst (Table 1). XRD analysis for all the spent Ni/CeO₂ catalysts (Fig. 10) generated diffraction peaks corresponding to metallic Ni and cubic ceria. There was no detectable signal due to NiO, suggesting the bulk Ni phase was in metallic state during the reaction. The diffraction peaks of metallic Ni for the spent Ni/CeO₂ did not become sharper relative to that observed for the activated samples pre-reaction (Fig. 2). This demonstrated Ni particles maintained a high dispersion without severe sintering due to strong interaction between Ni and CeO₂. Analysis of carbon deposition on Ni surface was further examined by TEM with associated images presented in Fig. 11. Significant amounts of carbon whisker were formed over Ni/CeO₂ for reactions using reduction temperature of 773 K (I) and 873 K (II). A number of Ni particles were encapsulated by the end of carbon whiskers, suggesting carbon generated on Ni surface with subsequent growth to whisker. We did not observe much amount of whisker type carbon over the spent Ni/CeO₂ for the reaction using reduction temperature of 973 K (III). TGA-DTG

Fig. 9. Variation of reaction rate (R_i; ■: CH₄, ●: CO₂) and H₂/CO (◇) as a function of inlet fractional concentration of (I) CH₄ (C [CH₄]) and (II) CO₂ (C [CO₂]) in dry reforming of methane over Ni/CeO₂. Reaction condition: T_{react} = 773 K, T_{reduce} = 773 K, P = 1 atm, GHSV = 4.8 × 10⁴ h⁻¹. Scatter: experimental data, line: fitting.

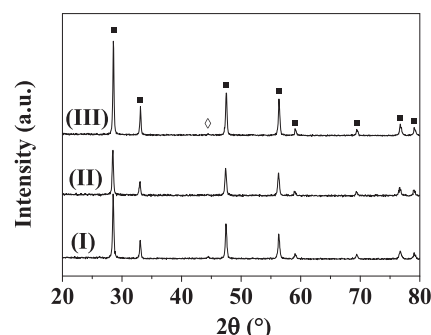


Fig. 10. XRD analysis of the spent Ni/CeO₂ catalysts (reduction temperature: (I) 773 K, (II) 873 K and (III) 973 K; ◇: Ni, ■: CeO₂).

analysis of the spent Ni/CeO₂ catalysts reduced at 773 K and 873 K (Fig. 12) revealed only one mass loss (7.3–15.4%) at ca. 875 K that can be attributed to combustion of whisker type carbon. This is in consistent with that (833–873 K) reported for the reaction over Ni/ZrO₂ [53] and Ni/CeO₂ [33]. There was no significant mass loss in the temperature range of 573–773 K that was characteristic of oxidation of amorphous or graphitic carbon. A calculation demonstrated the carbon deposition rates at 0.7–1.6 mmol_{carbon} g_{cat}⁻¹ h⁻¹ for both Ni/CeO₂ catalysts. In contrast, an increase (ca. 0.8%) in weight due to oxidation of metallic Ni (Ni → NiO) was recorded over the used Ni/CeO₂ (reduced at 973 K). We can note that the amount of carbon deposition was decreased with an increase in reduction temperature, suggesting a suppression of carbon formation. In dry reforming of methane over supported Ni catalysts, a large (> 2.5 nm) and free Ni surface facilitates carbon formation and particle agglomeration [54–56]. In this work, SMSI induced-decoration of Ni surface by a thin layer of ceria can inhibit carbon deposition. In addition, high oxygen mobility of the ceria layer can oxidise coke on Ni surface, notably at the metal-support interface boundary, contributing to lower carbon deposit. We demonstrated decoration of Ni surface via tuning metal-support interaction as an effective tool in controlling the catalytic activity of Ni/CeO₂ and carbon deposition in dry reforming of methane.

4. Conclusion

We have established the influence of metal-support interaction on the catalytic activity and carbon formation in dry reforming of methane to syngas over CeO₂ supported Ni nanoparticles. Reduction of Ni/CeO₂ at higher temperature (773 → 973 K) resulted in a loss in SSA (11 → 8 m² g⁻¹), surface Ni concentration (15.5% → 7.1%) and a stronger bonding between Ni and CeO₂ that inhibited severe agglomeration/sintering of Ni particles. Elevated reduction temperature (≥ 873 K) promoted migration of ceria from reduced support onto Ni surface, inducing decoration/encapsulation of Ni nanoparticles. The decoration/encapsulation effect decreased the catalyst capacity for adsorption/activation for CH₄ and CO₂ leading to lower conversion rates, but decreased carbon deposition in dry reforming of methane.

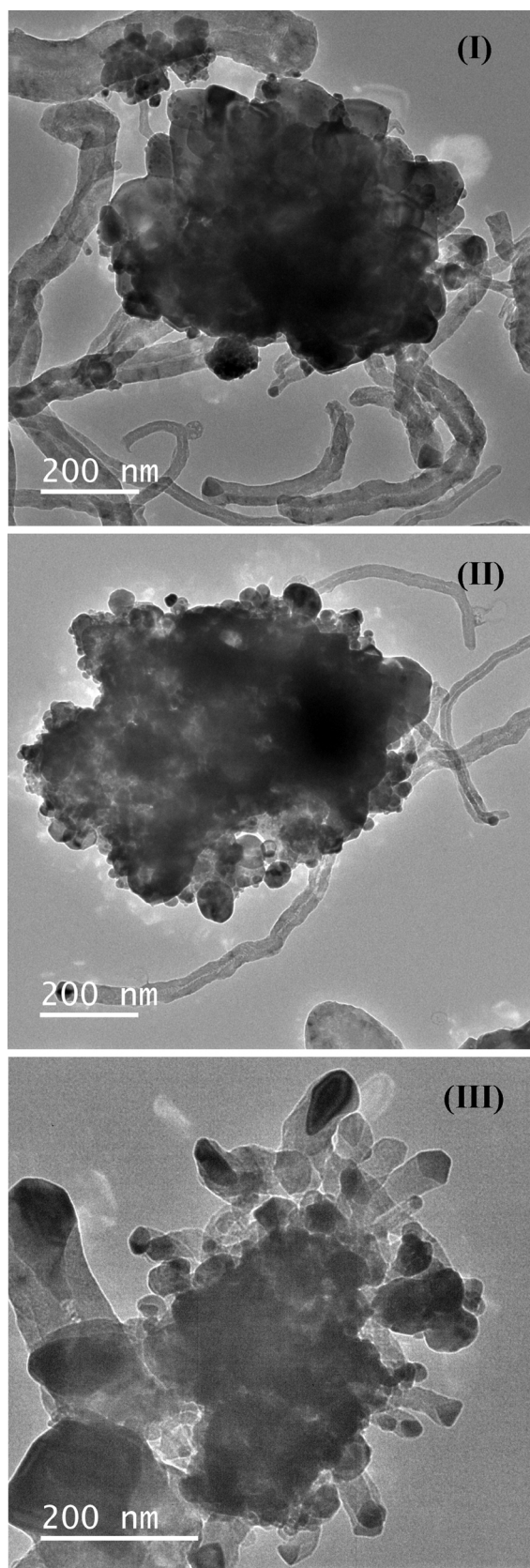


Fig. 11. Representative TEM images of the spent Ni/CeO₂ catalysts (reduction temperature: (I) 773 K, (II) 873 K and (III) 973 K).

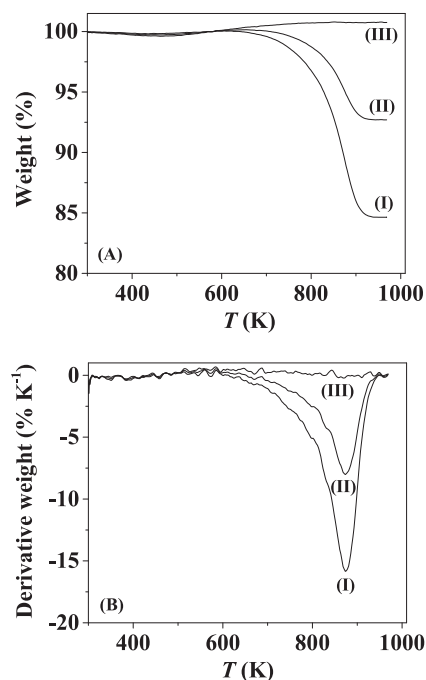


Fig. 12. (A) TGA and (B) DTG profiles of the spent Ni/CeO₂ catalysts (reduction temperature: (I) 773 K, (II) 873 K and (III) 973 K).

Acknowledgments

This work was financially supported by European Commission 7th Framework Programme: BIOGO project (Grant No. 604296). We thank Prof. Shanwen Tao and Mr. Lucas Tillman for their contribution to this work.

References

- [1] J.C. Matsubu, S.Y. Zhang, L. DeRita, N.S. Marinkovic, J.G.G. Chen, G.W. Graham, X.Q. Pan, P. Christopher, *Nat. Chem.* 9 (2017) 120–127.
- [2] J.A. Rodriguez, D.C. Grinter, Z.Y. Liu, R.M. Palomino, S.D. Senanayake, *Chem. Soc. Rev.* 46 (2017) 1824–1841.
- [3] M. Cargnello, V.V.T. Doan-Nguyen, T.R. Gordon, R.E. Diaz, E.A. Stach, R.J. Gorte, P. Fornasiero, C.B. Murray, *Science* 341 (2013) 771–773.
- [4] S. Gatla, D. Aubert, G. Agostini, O. Mathon, S. Pascarelli, T. Lunkenbein, M.G. Willinger, H. Kaper, *ACS Catal.* 6 (2016) 6151–6155.
- [5] Z.J. Mei, Y. Li, M.H. Fan, L. Zhao, J. Zhao, *Chem. Eng. J.* 259 (2015) 293–302.
- [6] T. Tabakova, F.B. Boccuzzi, M. Manzoli, D. Andreeva, *Appl. Catal. A: Gen.* 252 (2003) 385–397.
- [7] J.A. Rodriguez, P. Liu, D.J. Stacchiola, S.D. Senanayake, M.G. White, J.G.G. Chen, *ACS Catal.* 5 (2015) 6696–6706.
- [8] M. Garcia-Dieguez, E. Finocchio, M.A. Larrubia, L.J. Alemany, G. Busca, *J. Catal.* 274 (2010) 11–20.
- [9] D.C. Carvalho, H.S.A. de Souza, J.M. Filho, A.C. Oliveira, A. Campos, E.R.C. Milet, F.F. de Sousa, E. Padron-Hernandez, A.C. Oliveira, *Appl. Catal. A: Gen.* 473 (2014) 132–145.
- [10] F. Polo-Garzon, M. He, D.A. Bruce, *J. Catal.* 333 (2016) 59–70.
- [11] F. Polo-Garzon, D. Pakhare, J.J. Spivey, D.A. Bruce, *ACS Catal.* 6 (2016) 3826–3833.
- [12] F. Polo-Garzon, J.K. Scott, D.A. Bruce, *J. Catal.* 340 (2016) 196–204.
- [13] R.K. Singha, A. Yadav, A. Shukla, M. Kumar, R. Bal, *Catal. Commun.* 92 (2017) 19–22.
- [14] X.Y. Li, D. Li, H. Tian, L. Zeng, Z.J. Zhao, J.L. Gong, *Appl. Catal. B: Environ.* 202 (2017) 683–694.
- [15] A. Löfberg, J. Guerrero-Caballero, T. Kane, A. Rubbens, L. Jalowiecki-Duhamel, *Appl. Catal. B: Environ.* 212 (2017) 159–174.
- [16] M. Shirazi, E.C. Neyts, A. Bogaerts, *Appl. Catal. B: Environ.* 205 (2017) 605–614.
- [17] A. Tsoukalou, Q. Imtiaz, S.M. Kim, P.M. Abdala, S. Yoon, C.R. Muller, *J. Catal.* 343 (2016) 208–214.
- [18] B.V. Ayodele, M.R. Khan, C.K. Cheng, *Int. J. Hydrogen Energy* 41 (2016) 198–207.
- [19] P. Djinić, A. Pintar, *Appl. Catal. B: Environ.* 206 (2017) 675–682.
- [20] S.M. Kim, P.M. Abdala, T. Margossian, D. Hosseini, L. Foppa, A. Armutlulu, W. van Beek, A. Comas-Vives, C. Copéret, C. Muller, *J. Am. Chem. Soc.* 139 (2017) 1937–1949.
- [21] Q.X. Ma, J. Sun, X.H. Gao, J.L. Zhang, T.S. Zhao, Y. Yoneyama, N. Tsubaki, *Catal. Sci. Technol.* 6 (2016) 6542–6550.

- [22] T.D. Gould, M.M. Montemore, A.M. Lubers, L.D. Ellis, A.W. Weimer, J.L. Falconer, J.W. Medlin, *Appl. Catal. A: Gen.* 492 (2015) 107–116.
- [23] S. Kawi, Y. Kathiraser, J. Ni, U. Oemar, Z.W. Li, E.T. Saw, *ChemSusChem* 8 (2015) 3556–3575.
- [24] D. Pakhare, J. Spivey, *Chem. Soc. Rev.* 43 (2014) 7813–7837.
- [25] Z.Y. Liu, D.C. Grinter, P.G. Lustemberg, T.D. Nguyen-Phan, Y.H. Zhou, S. Luo, I. Waluyo, E.J. Crumlin, D.J. Stacchiola, J. Zhou, J. Carrasco, H.F. Busnengo, M.V. Ganduglia-Pirovano, S.D. Senanayake, J.A. Rodriguez, *Angew. Chem. Int. Ed.* 55 (2016) 7455–7459.
- [26] V.M. Gonzalez-Dela Cruz, J.P. Holgado, R. Pereñíguez, A. Caballero, *J. Catal.* 257 (2008) 307–314.
- [27] T. Komaya, A.T. Bell, Z. Wengsieh, R. Gronsky, F. Engelke, T.S. King, M. Pruski, *J. Catal.* 149 (1994) 142–148.
- [28] W. Jochum, D. Eder, G. Kaltenhauser, R. Kramer, *Top. Catal.* 46 (2007) 49–55.
- [29] J.Y. Park, L.R. Baker, G.A. Somorjai, *Chem. Rev.* 115 (2015) 2781–2817.
- [30] S. Bernal, J.J. Calvino, M.A. Cauqui, J.M. Gatica, C.L. Cartes, J.A.P. Omil, J.M. Pintado, *Catal. Today* 77 (2003) 385–406.
- [31] S.Y. Xiao, Z.Y. Meng, *J. Chem. Soc. Faraday Trans.* 90 (1994) 2591–2595.
- [32] N. Laosiripojana, S. Assabumrungrat, S. Charojrochkul, *Appl. Catal. A: Gen.* 327 (2007) 180–188.
- [33] H. Ay, D. Uner, *Appl. Catal. B: Environ.* 179 (2015) 128–138.
- [34] L. Katta, G. Thrumurthulu, B.M. Reddy, M. Muhler, W. Grunert, *Catal. Sci. Technol.* 1 (2011) 1645–1652.
- [35] F.J. Lin, R. Delmelle, T. Vinodkumar, B.M. Reddy, A. Wokaun, I. Alxneit, *Catal. Sci. Technol.* 5 (2015) 3556–3567.
- [36] T.S. Moraes, R.C.R. Neto, M.C. Ribeiro, L.V. Mattos, M. Kourtelesis, S. Ladas, X. Verykios, F.B. Noronha, *Appl. Catal. B: Environ.* 181 (2016) 754–768.
- [37] S. Mahammadunnisa, P.M.K. Reddy, N. Lingaiah, C. Subrahmanyam, *Catal. Sci. Technol.* 3 (2013) 730–736.
- [38] H.L. Tang, J.K. Wei, F. Liu, B.T. Qiao, X.L. Pan, L. Li, J.Y. Liu, J.H. Wang, T. Zhang, *J. Am. Chem. Soc.* 138 (2016) 56–59.
- [39] J.A. Farmer, C.T. Campbell, *Science* 329 (2010) 933–936.
- [40] X. Chen, M. Li, J.C. Guan, X.K. Wang, C.T. Williams, C.H. Liang, *Ind. Eng. Chem. Res.* 51 (2012) 3604–3611.
- [41] V.M. Shinde, G. Madras, *RSC Adv.* 4 (2014) 4817–4826.
- [42] M. Baron, O. Bondarchuk, D. Stacchiola, S. Shaikhutdinov, H.J. Freund, *J. Phys. Chem. C* 113 (2009) 6042–6049.
- [43] E. Beche, P. Charvin, D. Perarnau, S. Abanades, G. Flamant, *Appl. Catal. B: Environ.* 40 (2008) 264–267.
- [44] N. Wang, W.Z. Qian, W. Chu, F. Wei, *Catal. Sci. Technol.* 6 (2016) 3594–3605.
- [45] P.G. Lustemberg, P.J. Ramirez, Z.Y. Liu, R.A. Gutierrez, D.G. Grinter, J. Carrasco, S.D. Senanayake, J.A. Rodriguez, M.V. Ganduglia-Pirovano, *ACS Catal.* 6 (2016) 8184–8191.
- [46] F.G. Wang, L.L. Xu, J. Zhang, Y. Zhao, H. Li, H.X. Li, K. Wu, G.Q. Xu, W. Chen, *Appl. Catal. B: Environ.* 180 (2016) 511–520.
- [47] J.H. Bitter, K. Seshan, J.A. Lercher, *J. Catal.* 176 (1998) 93–101.
- [48] U. Oemar, Y. Kathiraser, L. Mo, X.K. Ho, S. Kawi, *Catal. Sci. Technol.* 6 (2016) 1173–1186.
- [49] S.B. Wang, G.Q. Lu, *Ind. Eng. Chem. Res.* 38 (1999) 2615–2625.
- [50] A. Nandini, K.K. Pant, S.C. Dhingra, *Appl. Catal. A: Gen.* 308 (2006) 119–127.
- [51] X.G. Zheng, S.Y. Tan, L.C. Dong, S.B. Li, H.M. Chen, *Chem. Eng. J.* 265 (2015) 147–156.
- [52] C. Pichas, P. Pomonis, D. Petrakis, A. Ladavos, *Appl. Catal. A: Gen.* 386 (2010) 116–123.
- [53] A. Wolfbeisser, O. Sophephun, J. Bernardi, J. Wittayakun, K. Föttinger, G. Rupprechter, *Catal. Today* 277 (2016) 234–245.
- [54] A. Rinaldi, J.P. Tessonnier, M.E. Schuster, R. Blume, F. Girgsdies, Q. Zhang, T. Jacob, S.B.A. Hamid, D.S. Su, R. Schlögl, *Angew. Chem. Int. Ed.* 50 (2011) 3313–3317.
- [55] K. Mette, S. Kuhl, A. Tarasov, M.G. Willinger, J. Krohnert, S. Wrabetz, A. Trunschke, M. Scherzer, F. Girgsdies, H. Dudder, K. Kahler, K.F. Ortega, M. Muhler, R. Schlögl, M. Behrens, T. Lunkenbein, *ACS Catal.* 6 (2016) 7238–7248.
- [56] H.S. Bengaard, J.K. Nørskov, J. Sehested, B.S. Clausen, L.P. Nielsen, A.M. Mølenbroek, J.R. Rostrup-Nielsen, *J. Catal.* 209 (2002) 365–384.